

## Theoretical Studies of Convectively Forced Mesoscale Flows in Three Dimensions. Part II: Shear Flow with a Critical Level

JI-YOUNG HAN AND JONG-JIN BAIK

*School of Earth and Environmental Sciences, Seoul National University, Seoul, South Korea*

(Manuscript received 18 February 2009, in final form 3 August 2009)

### ABSTRACT

Convectively forced mesoscale flows in a shear flow with a critical level are theoretically investigated by obtaining analytic solutions for a hydrostatic, nonrotating, inviscid, Boussinesq airflow system. The response to surface pulse heating shows that near the center of the moving mode, the magnitude of the vertical velocity becomes constant after some time, whereas the magnitudes of the vertical displacement and perturbation horizontal velocity increase linearly with time. It is confirmed from the solutions obtained in present and previous studies that this result is valid regardless of the basic-state wind profile and dimension. The response to 3D finite-depth steady heating representing latent heating due to cumulus convection shows that, unlike in two dimensions, a low-level updraft that is necessary to sustain deep convection always occurs at the heating center regardless of the intensity of vertical wind shear and the heating depth. For deep heating across a critical level, little change occurs in the perturbation field below the critical level, although the heating top height increases. This is because downward-propagating gravity waves induced by the heating above, but not near, the critical level can hardly affect the flow response field below the critical level. When the basic-state wind backs with height, the vertex of V-shaped perturbations above the heating top points to a direction rotated a little clockwise from the basic-state wind direction. This is because the V-shaped perturbations above the heating top is induced by upward-propagating gravity waves that have passed through the layer below where the basic-state wind direction is clockwise relative to that above.

### 1. Introduction

The characteristics of gravity waves produced in a stably stratified atmosphere strongly depend on environmental conditions such as basic-state wind speed and stability. The vertical wavelength of gravity waves, for example, becomes large for a stronger basic-state wind or a less stable atmosphere. In addition to the basic-state wind speed, the basic-state shear also has a significant influence on the characteristics of gravity waves.

The effect of mean wind variation with height on traveling internal gravity waves in a linear airflow system was studied by Bretherton (1966). He indicated that a wave group takes an infinite time to reach a critical level and thus nothing is transmitted. Note that the critical level is a level where the basic-state horizontal wind speed in the wave propagation direction is equal to

the horizontal propagation speed of waves. Booker and Bretherton (1967) showed that if the Richardson number [ $Ri = N^2/(dU/dz)^2$ , where  $N$  is the buoyancy frequency and  $U$  is the basic-state wind speed] is larger than  $1/4$ , a wave is transmitted, but its amplitude is attenuated by a factor of  $\exp[-\pi(Ri - 1/4)^{1/2}]$  on passage through the critical level. Jones (1968) found that incident waves can be overreflected if  $Ri$  is smaller than  $1/4$  near the critical level. In a nonlinear system, gravity waves near the critical level exhibit somewhat different behaviors from those in a linear system. Through nonlinear numerical simulations, Breeding (1971) indicated that if  $Ri$  is relatively large or smaller than  $1/4$ , the interaction of incident waves and the basic-state flow is similar to that predicted from the linear theory, but if  $Ri$  is small but larger than  $1/4$ , a large portion of the incident waves is reflected from the critical level, unlike the linear prediction.

The effect of wind shear on gravity waves induced by thermal forcing has been studied theoretically to better understand thermally forced mesoscale flows. However, unlike theoretical studies of orographically forced flows, many of which deal with a three-dimensional (3D)

---

*Corresponding author address:* Jong-Jin Baik, School of Earth and Environmental Sciences, Seoul National University, Seoul 151-742, South Korea.  
E-mail: jjbaik@snu.ac.kr

airflow system (e.g., Grubišić and Smolarkiewicz 1997; Shutts 1998), studies that consider the shear flow in the presence of a 3D heat source are very limited (Lin and Li 1988). Lin (1987) obtained a solution for a two-dimensional (2D), steady-state problem with isolated or differential heating, showing that the phase relationship between the thermal forcing whose top is below the critical level and the induced vertical motion at the low level may be positive or negative depending on Ri and the depth of heating layer. He also showed that in response to the heating in the vicinity of the critical level, the flow near the heat source is dominated by an upward motion for a wide range of Ri. By examining a 3D steady-state response of a stratified shear flow to elevated heating, Lin and Li (1988) suggested that the formation of V-shaped cloud tops is caused by the action of the mean wind on upward-propagating waves generated by the thermal forcing.

Examining transient behaviors in the presence of basic-state shear is important to extend our understanding of thermally forced flows. The transient critical-level effect for internal gravity waves was studied by Baik et al. (1999a). They solved a 2D transient problem with line-type pulse forcing analytically and showed that a spatially and temporally dependent attenuation factor exists because internal gravity waves passing through any point at any time consist of waves that have already experienced the transient critical-level effect and those that have not experienced the effect yet. Baik et al. (1999b) also examined the 2D transient dynamics of a shear flow with diabatic forcing and found that the flow response field to the steady forcing is composed of a stationary mode, which develops and stays near the steady forcing region, and a moving mode, whose center travels downstream with a speed of the basic-state wind. Recently, Song and Chun (2005) analytically formulated the phase-speed spectrum of the momentum flux of convectively generated internal gravity waves in 2D and 3D airflow systems with low-level wind shear and confirmed that the analytic spectrum can reproduce the numerically simulated momentum flux spectra reasonably well.

To understand thermally forced mesoscale flows, which include not only quasi-2D squall lines but also 3D mesoscale convective systems, it is necessary to consider a 3D airflow system (Skamarock et al. 1994). However, to the best of our knowledge, there is no study that has obtained analytic solutions to a 3D transient problem in a shear flow in physical space. Here, as an extension of the uniform basic-state flow case (Han and Baik 2009, hereafter Part I), we obtain analytic solutions to a 3D transient problem in a shear flow with a critical level. The main purpose of the present paper is to theoretically examine the linear dynamics of convectively forced mesoscale flows

in a shear flow using our 3D transient solutions. In particular, we try to understand the characteristics of stationary and moving modes in a shear flow, the critical-level effect, and the effect of varying basic-state wind direction with height on induced mesoscale circulation. Section 2 describes governing equations and solutions. Section 3 presents analysis results of the solutions. A summary and conclusions are given in section 4.

## 2. Governing equations and solutions

Consider a nonrotating, inviscid airflow system satisfying the hydrostatic and Boussinesq approximations. Equations governing small-amplitude perturbations in a basic-state flow with diabatic forcing can be written as follows (e.g., Lin 2007):

$$\frac{\partial u}{\partial t} + U \frac{\partial u}{\partial x} + V \frac{\partial u}{\partial y} + w \frac{dU}{dz} = -\frac{\partial \pi}{\partial x}, \quad (1)$$

$$\frac{\partial v}{\partial t} + U \frac{\partial v}{\partial x} + V \frac{\partial v}{\partial y} + w \frac{dV}{dz} = -\frac{\partial \pi}{\partial y}, \quad (2)$$

$$\frac{\partial \pi}{\partial z} = b, \quad (3)$$

$$\frac{\partial b}{\partial t} + U \frac{\partial b}{\partial x} + V \frac{\partial b}{\partial y} + N^2 w = \frac{g}{c_p T_0} q, \quad (4)$$

$$\frac{\partial u}{\partial x} + \frac{\partial v}{\partial y} + \frac{\partial w}{\partial z} = 0, \quad (5)$$

where  $u$ ,  $v$ , and  $w$  are the perturbation velocities in the  $x$ ,  $y$ , and  $z$  directions, respectively;  $\pi$  ( $=p/\rho_0$ , where  $p$  is the perturbation pressure and  $\rho_0$  is the reference density) is the perturbation kinematic pressure;  $b$  ( $=g\theta/\theta_0$ , where  $g$  is the gravitational acceleration,  $\theta$  is the perturbation potential temperature, and  $\theta_0$  is the reference potential temperature) is the perturbation buoyancy;  $U$  and  $V$  are the basic-state wind velocities in the  $x$  and  $y$  directions, respectively;  $N$  is the buoyancy frequency;  $c_p$  is the specific heat of air at constant pressure;  $T_0$  is the reference temperature; and  $q$  is the diabatic forcing. Here, a constant stratification is considered and the basic-state horizontal wind is assumed to have a constant vertical wind shear:

$$U(z) = U_0 - \alpha z, \quad (6a)$$

$$V(z) = V_0 - \beta z, \quad (6b)$$

where  $U_0$  and  $V_0$  are  $x$ - and  $y$ -directional basic-state horizontal wind speeds at the surface, respectively, and  $\alpha$  and  $\beta$  are the constant vertical wind shears of  $U$  and  $V$ , respectively. The structure of surface pulse forcing is the same as in Part I:

$$q(x, y, z, t) = q_0 \frac{1}{[(x/a_x)^2 + (y/a_y)^2 + 1]^{3/2}} \delta(z-h) \delta(t), \quad (7)$$

where  $q_0$  is the amplitude of the diabatic forcing,  $a_x$  and  $a_y$  determine the horizontal sizes of the diabatic forcing in the  $x$  and  $y$  directions, respectively,  $\delta$  is the Dirac delta function, and  $h$  is the height where the surface forcing is applied. Using the Green function method, the solution to the finite-depth steady forcing, which represents latent heat released by deep moist convection, is obtained by integrating the solution to the above surface pulse forcing with respect to forcing level and time. Figure 1 depicts the schematic diagrams of the basic-state wind profile and diabatic forcing in the surface and finite-depth forcing cases.

Combining the above governing equations into a single equation for the perturbation vertical velocity gives

$$\left( \frac{\partial}{\partial t} + U \frac{\partial}{\partial x} + V \frac{\partial}{\partial y} \right)^2 \frac{\partial^2 w}{\partial z^2} + N^2 \left( \frac{\partial^2 w}{\partial x^2} + \frac{\partial^2 w}{\partial y^2} \right) = \frac{g}{c_p T_0} \left( \frac{\partial^2 q}{\partial x^2} + \frac{\partial^2 q}{\partial y^2} \right). \quad (8)$$

Applying the double Fourier transform in  $x$  ( $\rightarrow k$ ) and  $y$  ( $\rightarrow l$ ) and the Laplace transform in  $t$  ( $\rightarrow s$ ) to (8) yields

$$\frac{d^2 \hat{w}}{dz^2} + N^2 \lambda^2 \hat{w} = \frac{g}{c_p T_0} \lambda^2 \hat{q}, \quad (9)$$

where

$$\hat{w}_1(k, l, z, s) = C_1 \frac{(ik)^2 + (il)^2}{2i\mu'(ik\alpha + il\beta)} e^{-\sqrt{k^2 a_x^2 + l^2 a_y^2}} (S_h^{-3/2-i\mu'} S_z^{1/2+i\mu'} - S_h^{-3/2-i\mu'} S_0^{2i\mu'} S_z^{1/2-i\mu'}) \quad \text{for } 0 \leq z \leq h, \quad (12a)$$

$$\hat{w}_2(k, l, z, s) = C_1 \frac{(ik)^2 + (il)^2}{2i\mu'(ik\alpha + il\beta)} e^{-\sqrt{k^2 a_x^2 + l^2 a_y^2}} (S_h^{-3/2+i\mu'} S_z^{1/2-i\mu'} - S_h^{-3/2-i\mu'} S_0^{2i\mu'} S_z^{1/2-i\mu'}) \quad \text{for } z > h, \quad (12b)$$

where

$$C_1 = \frac{g q_0 a_x a_y}{2\pi c_p T_0}, \quad S_h = s + ikU_h + ilV_h,$$

$$S_0 = s + ikU_0 + ilV_0, \quad U_h = U_0 - \alpha h,$$

$$V_h = V_0 - \beta h.$$

The solution in physical space is obtained by applying the inverse Laplace transform and the inverse double

$$\lambda^2 = \frac{(ik)^2 + (il)^2}{(s + ikU + ilV)^2}, \quad \hat{q} = q_0 \frac{a_x a_y}{2\pi} e^{-\sqrt{k^2 a_x^2 + l^2 a_y^2}} \delta(z-h).$$

The general solution of (9) is

$$\hat{w}_1(k, l, z, s) = A_1(k, l, s) S_z^{1/2+i\mu'} + B_1(k, l, s) S_z^{1/2-i\mu'} \quad \text{for } 0 \leq z \leq h, \quad (10a)$$

$$\hat{w}_2(k, l, z, s) = A_2(k, l, s) S_z^{1/2+i\mu'} + B_2(k, l, s) S_z^{1/2-i\mu'} \quad \text{for } z > h, \quad (10b)$$

where

$$S_z = s + ikU + ilV,$$

$$\mu' = \text{sgn}(k\alpha + l\beta) \left[ \frac{k^2 + l^2}{(k\alpha + l\beta)^2} N^2 - \frac{1}{4} \right]^{1/2}.$$

By imposing a flat bottom boundary condition [ $\hat{w}_1(k, l, z, s) = 0$  at  $z = 0$ ], an upper radiation condition [ $A_2(k, l, s) = 0$ ], and two boundary conditions at the interface  $z = h$  given by

$$\frac{d\hat{w}_2}{dz} - \frac{d\hat{w}_1}{dz} = \frac{g q_0 a_x a_y}{2\pi c_p T_0} \lambda^2 e^{-\sqrt{k^2 a_x^2 + l^2 a_y^2}}, \quad (11a)$$

$$\hat{w}_2 - \hat{w}_1 = 0, \quad (11b)$$

the coefficients  $A_1(k, l, s)$ ,  $B_1(k, l, s)$ ,  $A_2(k, l, s)$ , and  $B_2(k, l, s)$  are determined. Then, the solution in transformed space becomes

Fourier transform upon (12). Some details are given in the appendix.

### 3. Results and discussion

#### a. Surface pulse heating case

Figure 2 shows the time evolution of the perturbation vertical velocity field along  $y = 0$  in a constant unidirectional shear flow with surface pulse heating. The heating is applied at  $z = 1$  km. The specified parameter values

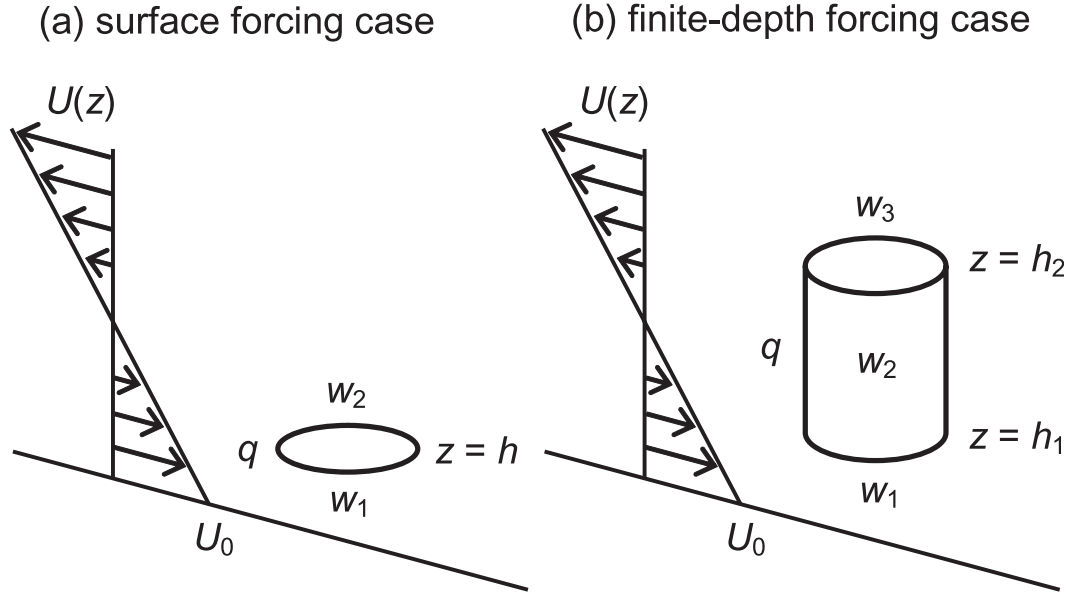


FIG. 1. Schematic diagrams of the basic-state wind profile and diabatic forcing in a constant unidirectional shear flow with (a) surface and (b) finite-depth forcing.

for the basic-state wind profile are  $U_0 = 12.5 \text{ m s}^{-1}$ ,  $\alpha = 0.0025 \text{ s}^{-1}$ ,  $V_0 = 0 \text{ m s}^{-1}$ , and  $\beta = 0 \text{ s}^{-1}$  (Table 1). Therefore, the wind reversal level  $z_c$ , which is a critical level for internal gravity waves with zero horizontal phase speeds, is located at  $z = 5 \text{ km}$  and the basic-state wind speed at the surface heating height of  $z = 1 \text{ km}$  ( $U_h$ ) is  $10 \text{ m s}^{-1}$ . The values of other parameters are  $N = 0.01 \text{ s}^{-1}$ ,  $T_0 = 273 \text{ K}$ ,  $q_0 = 2 \text{ J m kg}^{-1}$ , and  $a_x = a_y = 10 \text{ km}$ . The initial response to the surface pulse heating is a vertically extended upward motion, which is concentrated near the heating center, and a very weak compensating downward motion, which occurs in the rest of the region (Fig. 2a). As time progresses, the initial updraft region above the surface forcing height tilts upstream and downstream. Above the surface forcing height, alternating downdraft and updraft with upstream and downstream tilts are produced as in the uniform flow case of Part I. However, the flow field in the shear flow case is not axisymmetric, unlike the uniform flow case in which the flow field is axisymmetric around a moving axis of  $x = U_{ht}$  and  $y = 0$  (dotted gray line in Fig. 2f).

Baik et al. (1999a,b) examined the transient critical-level effect for internal gravity waves in a 2D transient framework, showing that the amplitude of gravity waves that have passed through the transient critical level is attenuated. In three dimensions, the transient critical level  $z_{ct}$  for internal gravity waves that originate at the initial forcing center  $x = y = 0$  is the level where  $\theta_z$  in the attenuation factor  $[e^{\pm(\theta_h - \theta_z)\mu'}]$  in (A5)] changes its sign. That is,

$$z_{ct} = \frac{1}{\alpha} \left( U_0 - \frac{x + y \tan \theta}{t} \right). \quad (13)$$

The transient critical level  $z_{ct}$  is indicated by the dashed-dotted gray line in Fig. 2f. Note that for  $y = 0$  or waves whose wave fronts are perpendicular to the basic-state wind direction ( $\tan \theta = 0$ ), the transient critical level in three dimensions is equal to that in two dimensions [ $z_{ct} = (U_0 - x/t)/\alpha$ ; Eq. (18) in Baik et al. (1999b)]. The amplitude of gravity waves that have passed through the transient critical level (i.e., in regions of  $z > z_{ct}$  and  $x + y \tan \theta < U_{ht}$  and of  $z < z_{ct}$  and  $x + y \tan \theta > U_{ht}$ , where  $\theta_z$  and  $\theta_h$  have opposite signs and hence the attenuation factor becomes very small) is much weaker than that in the rest of the region (Fig. 2f).

For large  $t$ , the transient critical level gets close to the critical level for internal gravity waves in a steady state. With thermal forcing applied below the critical level, the attenuation factor for upward-propagating gravity waves that come directly from the thermal forcing  $[e^{(-\theta_h + \theta_z)\mu'}]$  in (A5b)] approaches 1 as  $t \rightarrow \infty$  for finite values of  $x$  and  $y$  below the critical level. On the other hand, above the critical level,  $e^{(-\theta_h + \theta_z)\mu'}$  approaches  $\exp\{-\pi[(\text{Ri}/\cos^2 \theta) - 1/4]^{1/2}\}$  as  $t \rightarrow \infty$  for finite values of  $x$  and  $y$ . The result that waves passing through the critical level in a steady-state limit are attenuated by a factor of  $\exp\{-\pi[(\text{Ri}/\cos^2 \theta) - 1/4]^{1/2}\}$  is consistent with the result of a steady-state study on orographic gravity waves by Grubišić and Smolarkiewicz (1997). In a steady state, waves whose wave fronts are more parallel to the basic-state wind direction (i.e., waves with smaller values of

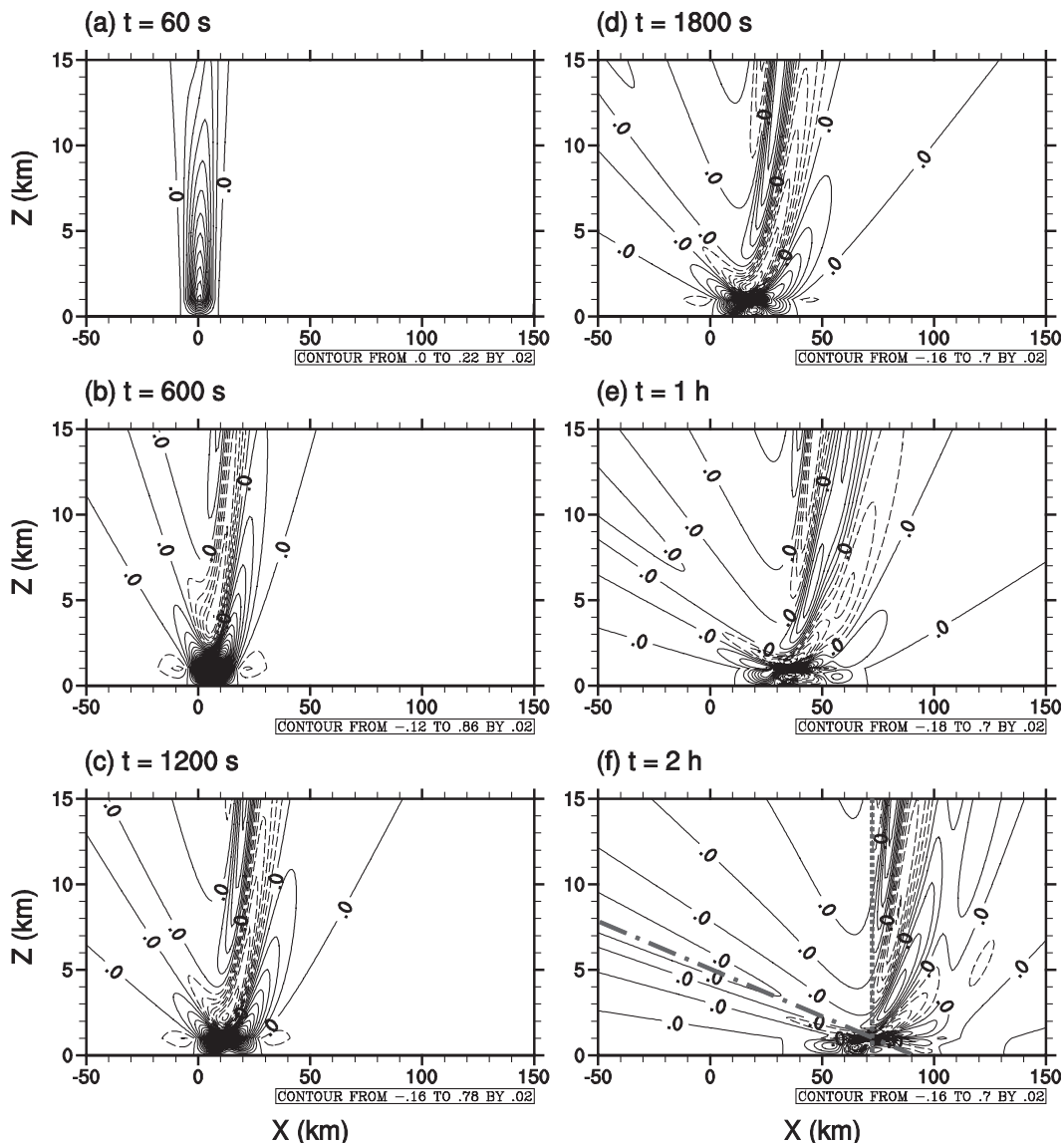


FIG. 2. The time evolution of the perturbation vertical velocity field along  $y = 0$  in a constant unidirectional shear flow with surface pulse heating applied at  $z = 1$  km:  $t =$  (a) 60 s, (b) 600 s, (c) 1200 s, (d) 1800 s, (e) 1 h, and (f) 2 h. The specified parameter values are  $U_0 = 12.5 \text{ m s}^{-1}$ ,  $\alpha = 0.0025 \text{ s}^{-1}$ ,  $V_0 = 0 \text{ m s}^{-1}$ ,  $\beta = 0 \text{ s}^{-1}$ ,  $N = 0.01 \text{ s}^{-1}$ ,  $T_0 = 273 \text{ K}$ ,  $q_0 = 2 \text{ J m kg}^{-1}$ , and  $a_x = a_y = 10 \text{ km}$ . The heating center is located at  $(x, y, z) = (0 \text{ km}, 0 \text{ km}, 1 \text{ km})$ . The values are scaled by  $10^6$  and the actual contour interval is  $2 \times 10^{-8} \text{ m s}^{-1}$ . The dashed lines represent the negative values. The moving axis that propagates downwind with a speed equal to the basic-state wind speed at the forcing level ( $x = U_0 t$ ) and the transient critical level for internal gravity waves originating at the initial forcing center [ $z_{ct} = \{U_0 - (x + y \tan \theta)/t\}/\alpha$ ] are indicated by the dotted and dashed-dotted gray lines in Fig. 2f, respectively.

$|\cos \theta|$ ) are more effectively absorbed at the critical level, and waves whose wave fronts are in the basic-state wind direction (i.e., waves with  $\cos \theta = 0$ ) are completely absorbed (Grubišić and Smolarkiewicz 1997).

In the uniform flow case (Part I), it is confirmed from the solution [ $e^{-(N|z-h|/X)\cos \theta}$  term in Eq. (A7) of Part I] that the magnitude of the vertical velocity decreases exponentially in the vertical away from the surface forcing

height and hence becomes very small in the region not close to the surface forcing height (see Fig. 1d of Part I). In the shear flow case, however, the magnitude of the vertical velocity is relatively large in the region where gravity waves originating at the initial forcing center do not pass through the transient critical level (i.e., in regions of  $z > z_{ct}$  and  $x + y \tan \theta > U_0 t$  and of  $z < z_{ct}$  and  $x + y \tan \theta < U_0 t$ ; see Fig. 2). This difference is because



TABLE 1. Parameter values considered in the case of a constant unidirectional shear flow with surface pulse heating or finite-depth steady heating.

Parameter	Value
$x$ -directional basic-state horizontal wind speed at the surface ( $U_0$ )	12.5 m s <sup>-1</sup>
$y$ -directional basic-state horizontal wind speed at the surface ( $V_0$ )	0 m s <sup>-1</sup>
Vertical wind shear of the $x$ -directional basic-state horizontal wind ( $\alpha$ )	0.0025 s <sup>-1</sup>
Vertical wind shear of the $y$ -directional basic-state horizontal wind ( $\beta$ )	0 s <sup>-1</sup>
Buoyancy frequency ( $N$ )	0.01 s <sup>-1</sup>
Reference temperature ( $T_0$ )	273 K
Parameter that determines the $x$ -directional horizontal size of the thermal forcing ( $a_x$ )	10 km
Parameter that determines the $y$ -directional horizontal size of the thermal forcing ( $a_y$ )	10 km

the vertical wind shear acts as an additional source of wave energy in a shear flow by converting the kinetic energy of the basic-state flow into perturbation wave energy (Eliassen and Palm 1960).

As in the uniform flow case, the magnitude of the maximum upward motion observed at the center of the moving mode remains constant after some time (Figs. 2d–f). Therefore, the magnitude of the vertical displacement at the center of the moving mode increases linearly as time progresses. This is apparent from the solution for the perturbation vertical velocity to the surface pulse forcing [Eq. (A5a)]. The solution shows that in a shear flow with an unbounded domain below [retaining only the terms multiplied by  $e^{(\theta_h - \theta_z)\mu'}$ ],

$$w_{3D,p}(U_h t, 0, h, t) \rightarrow \frac{FN}{\alpha\mu\pi} 2K\left(-\frac{1}{4\mu^2}\right) \quad \text{for large } t, \quad (14)$$

where  $F = gq_0/(c_p T_0 a_x N)$ ,  $\mu = (\text{Ri} - 1/4)^{1/2}$ , and  $K(m)$  is the complete elliptic integral of the first kind. When  $\alpha = 0$ , the value that the vertical velocity at the center of the moving mode converges to is equal to that in the uniform flow case of Part I (i.e.,  $F$ ). It is also confirmed from the solution for the perturbation horizontal velocity that the magnitude of the perturbation horizontal velocity increases linearly with time near the center of the moving mode. Based on the results of present and previous studies, it is concluded that the magnitude of the vertical velocity remains constant after some time at the center of the moving mode, whereas the magnitudes of the vertical displacement and perturbation horizontal velocity increase linearly with time near the center of the moving mode. This finding is valid regardless of whether the basic-state horizontal wind is uniform with height or

has a constant vertical wind shear and whether the air-flow system considered is 2D or 3D.

### b. Finite-depth steady heating case

Figure 3 shows the time evolution of the perturbation vertical velocity field along  $y = 0$  in a constant unidirectional shear flow with finite-depth steady heating. The heating, which is regarded as representing latent heat release in long-lived moist convection, is specified uniformly in the vertical from  $z = 1$  to 9 km and is steadily applied. The specified parameter values in the finite-depth steady heating case are the same as those in the surface pulse heating case (Table 1) except for  $q_0 = 2 \text{ J kg}^{-1} \text{ s}^{-1}$ . At the initial stage, there is an upward motion that extends vertically near the heating center with a weak compensating downward motion in its surroundings (Fig. 3a). As time progresses, the field of stationary gravity waves develops into a strong updraft extending over the steady heating layer and alternating downdrafts and updrafts with an upstream tilt above the heating top. The strong updraft stands more upright than that in a uniform flow (Part I). After  $t = 1 \text{ h}$ , in addition to two local maxima observed in the upper and lower parts of the strong updraft region, more local maxima are produced near the wind reversal level where the vertical wavelength of gravity waves becomes small. As the vertical wind shear decreases, more local maxima appear within the strong updraft (Lin 1987). This is because internal gravity waves with shorter vertical wavelengths are produced in the strong updraft region as the vertical wind shear decreases. In a shear flow with thermal forcing located across the wind reversal level, the moving mode consists of leftward-propagating and rightward-propagating perturbation groups, which are induced by thermal forcing above and below the wind reversal level, respectively. At  $t = 2 \text{ h}$ , both moving modes with weak intensities are observed near the boundaries of Fig. 3e. After the moving modes propagate far away from the steady heating region, the pattern of the stationary mode is almost unchanged with time (Figs. 3e,f).

The perturbation vertical velocity fields at various heights at  $t = 2 \text{ h}$  are shown in Fig. 4. At the heating bottom (and also below the heating bottom), the initial circular upward motion develops into a V-shaped upward motion (Fig. 4a). In much of the steady heating layer, especially at the wind reversal level, a nearly circular upward motion is observed near the heating center at all times (Fig. 4b). Above the heating top, V-shaped perturbations are produced, just as below the heating bottom. At  $z = 10 \text{ km}$  (Fig. 4c), V-shaped upward and downward motions with similar intensities develop on the upwind and downwind sides of the heating center,

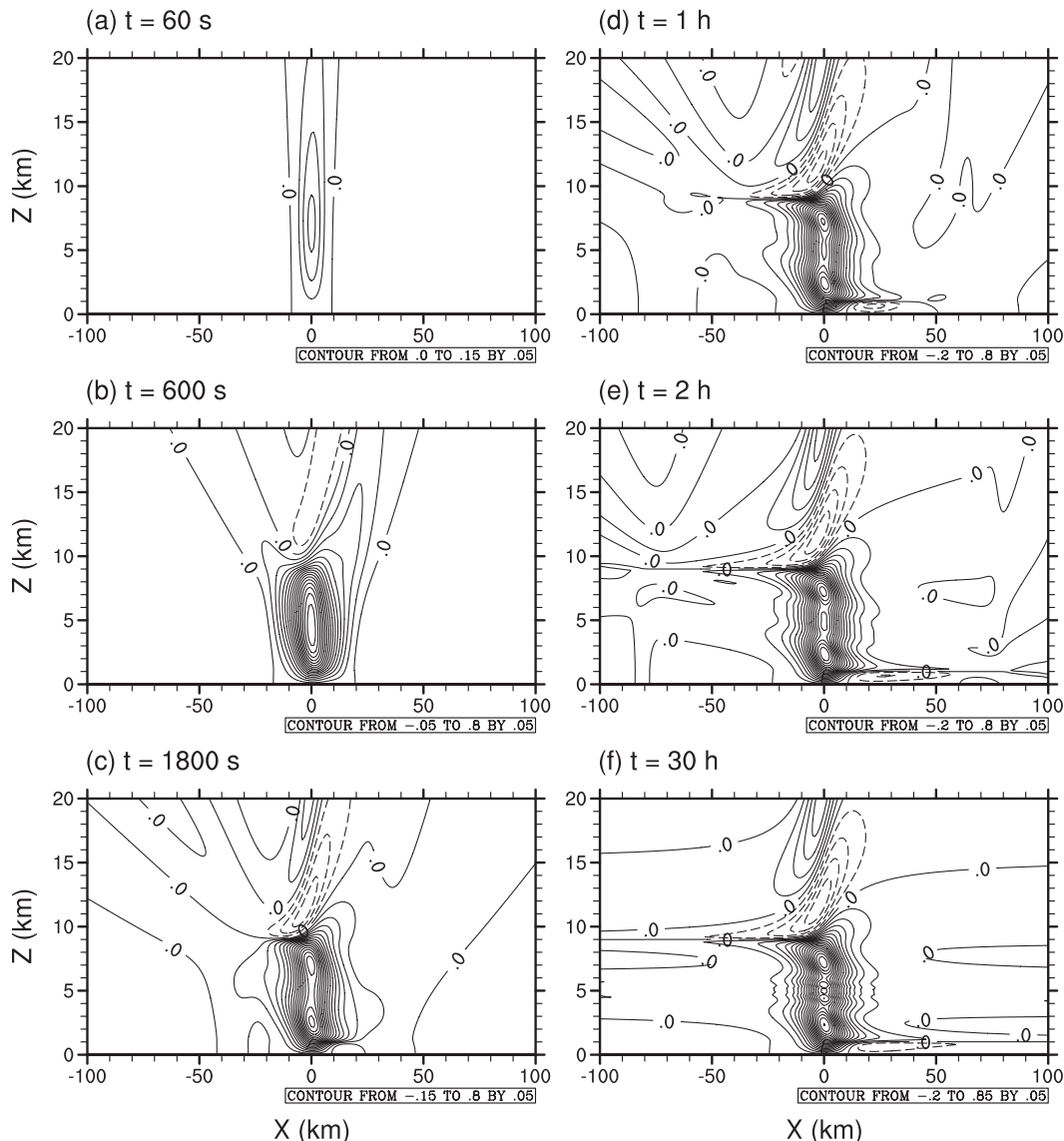


FIG. 3. The time evolution of the perturbation vertical velocity field along  $y = 0$  in a constant unidirectional shear flow with finite-depth steady heating applied uniformly in the vertical from  $z = 1$  to  $9$  km:  $t =$  (a)  $60$  s, (b)  $600$  s, (c)  $1800$  s, (d)  $1$  h, (e)  $2$  h, and (f)  $30$  h. The specified parameter values in the finite-depth steady heating case are the same as those in the surface pulse heating case (Table 1) except for  $q_0 = 2 \text{ J kg}^{-1} \text{ s}^{-1}$ . The contour interval is  $0.05 \text{ m s}^{-1}$ .

respectively. At  $z = 14$  km (Fig. 4d), an upwind upward motion with much weaker intensity is located farther in the upstream direction and V-shaped downward and upward motions, which become broader in the direction perpendicular to the basic-state wind, are located upwind and downwind of the heating center, respectively. Similar V-shaped features were also observed in a constant unidirectional shear flow past an isolated mountain below the critical level; this was explained using an asymptotic solution at a large distance from a mountain (Grubišić and Smolarkiewicz 1997). Grubišić and Smolarkiewicz

(1997) showed that waves below the critical level are confined to the paraboloidal envelopes, which get wider with height in the direction perpendicular to the basic-state wind, as in a uniform flow, but the wave envelopes are wider than those in a uniform flow at all heights.

Figure 5 shows the vertical variations of the vertical flux of the zonal momentum integrated over the horizontal plane ( $\overline{uw}$ , where the overbar denotes an integration over the  $x$ - $y$  plane) at  $t = 600$  s,  $1800$  s,  $1$  h, and  $2$  h. In a constant unidirectional shear flow with deep heating across the wind reversal level, the momentum

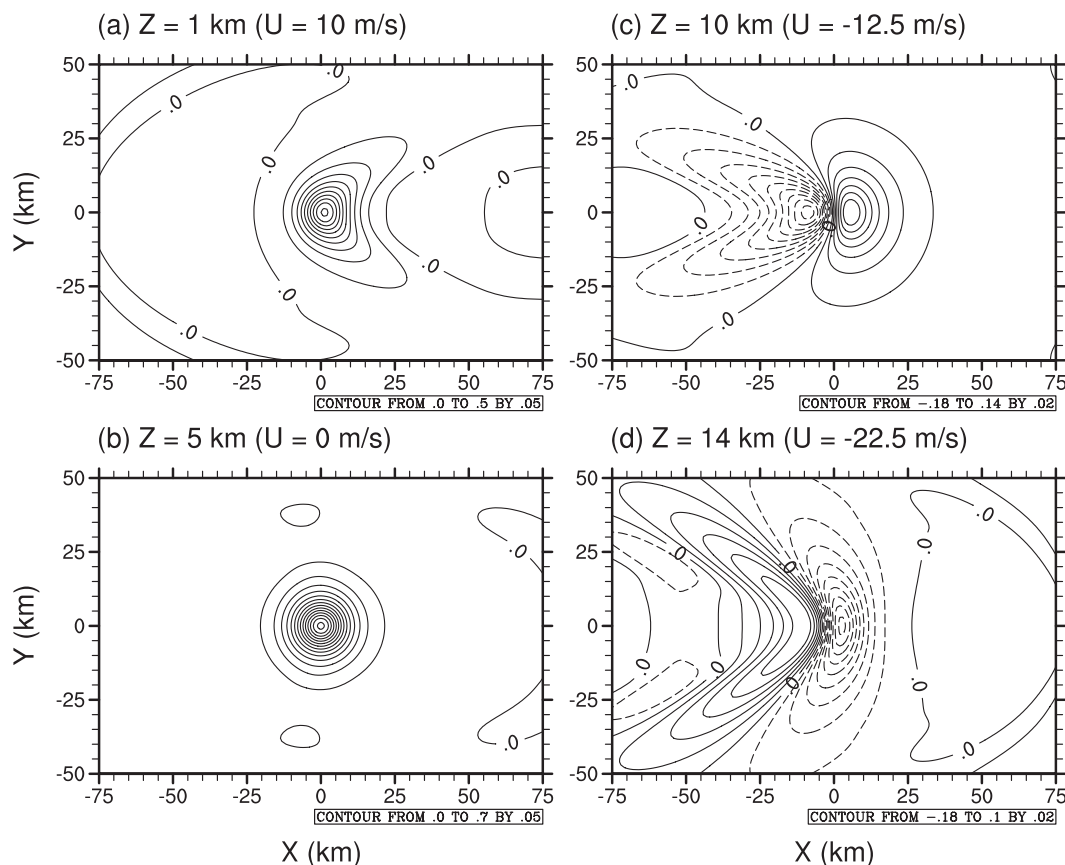


FIG. 4. The perturbation vertical velocity fields at heights of  $z$  = (a) 1, (b) 5, (c) 10, and (d) 14 km at  $t = 2$  h in a constant unidirectional shear flow with finite-depth steady heating applied uniformly in the vertical from  $z = 1$  to 9 km. The contour intervals are  $0.05 \text{ m s}^{-1}$  in (a) and (b) and  $0.02 \text{ m s}^{-1}$  in (c) and (d).

flux is positive at all times except for  $t = 0$  where  $u = w = 0$  and at all levels except for the surface where  $w = 0$ . This is in contrast to the momentum flux in the corresponding 2D case. In two dimensions, the momentum flux is negative in large parts of the heating layer (e.g., Lin 1987). This difference in the sign of the momentum flux in the heating layer is due to a difference in the field of  $x$ -directional perturbation velocity (Fig. 6). In three dimensions, the region of strong positive  $x$ -directional perturbation velocity, which is elongated in the basic-state wind direction, is located near the concentrated heating region where strong upward motion exists (Fig. 6b). In two dimensions, there is a relatively weak negative  $x$ -directional perturbation velocity in the steady heating layer (Fig. 6a).

The initial momentum flux in three dimensions increases with height up to the heating top and then decreases (solid line in Fig. 5). As the strong updraft extending over the steady heating layer develops, layers of decreasing momentum flux with height are produced in the lower part of the heating layer and above the wind

reversal level. At  $t = 1$  h and 2 h, the maximum momentum flux appears at the wind reversal level. This is because the maximum perturbation vertical velocity coincides with the maximum  $x$ -directional perturbation velocity at the wind reversal level and heating center  $(x, y, z) = (0 \text{ km}, 0 \text{ km}, 5 \text{ km})$ . Let the  $x$  direction be the east–west direction. The increase in the momentum flux with height (i.e., the vertical divergence of the momentum flux) below the wind reversal level, where the westerly basic-state wind exists, results in a decrease in the westerly basic-state wind. On the other hand, the decrease in the momentum flux with height (i.e., the vertical convergence of the momentum flux) above the wind reversal level, where the easterly basic-state wind exists, leads to a decrease in the easterly basic-state wind. The arrows in Fig. 5 indicate the layers of mean flow deceleration that can result from the vertical convergence/divergence of the momentum flux at  $t = 2$  h. The mean flow deceleration occurs in regions similar to those in the uniform flow case (i.e., below, above, and in the middle region of the heating layer). In the shear flow case, however, the



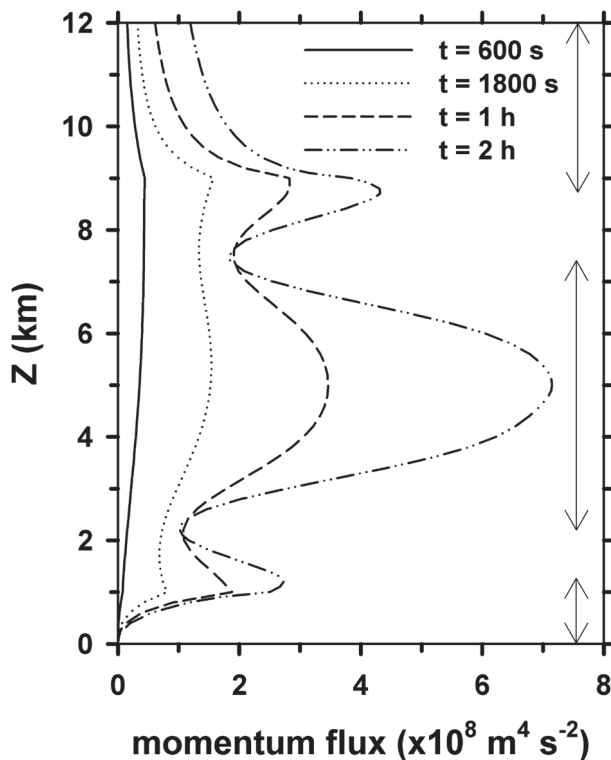


FIG. 5. The vertical variations of the vertical flux of the zonal momentum integrated over the horizontal plane ( $\text{m}^4 \text{s}^{-2}$ ) at  $t = 600 \text{ s}$ ,  $1800 \text{ s}$ ,  $1 \text{ h}$ , and  $2 \text{ h}$  in a constant unidirectional shear flow with finite-depth steady heating applied uniformly in the vertical from  $z = 1$  to  $9 \text{ km}$ . The layers of mean flow deceleration that can result from the vertical convergence/divergence of the momentum flux at  $t = 2 \text{ h}$  are indicated by arrows on the right side of the figure.

mean flow deceleration is also observed right above the heating bottom and right below the heating top.

Figure 7 shows the perturbation vertical velocity at the heating center ( $x = 0 \text{ km}$ ) and heating bottom height ( $z = 1 \text{ km}$ ) at  $t = 2 \text{ h}$  as a function of  $\text{Ri}$  ( $=N^2/\alpha^2$ ) and the heating depth nondimensionalized by the critical level height  $[(h_2 - h_1)/z_c]$  in two and three (at  $y = 0 \text{ km}$ ) dimensions. The heating depth and  $\text{Ri}$  are varied by changing heating top height and vertical wind shear, respectively. In two dimensions with a bounded domain below, as shown in a steady-state study by Lin (1987), a low-level upward or downward motion occurs at the heating center depending on the intensity of vertical wind shear and the heating depth except for the initial stage. Note that a low-level downward motion can appear at the heating center when a low-level downward motion produced by reflected upward-propagating gravity waves is strong enough to overcome a low-level upward motion induced directly by the heating. At early times, the downward motion is observed at the heating center only for low- $\text{Ri}$  flow with steady heating below

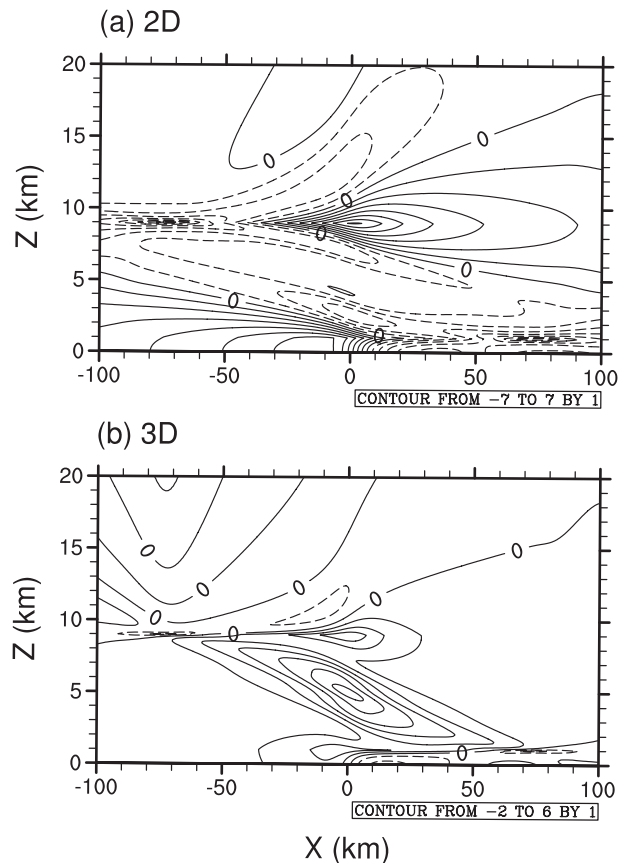


FIG. 6. The  $x$ -directional perturbation velocity fields at  $t = 2 \text{ h}$  in a constant unidirectional shear flow with finite-depth steady heating applied uniformly in the vertical from  $z = 1$  to  $9 \text{ km}$  in (a) two and (b) three (along  $y = 0$ ) dimensions. The contour interval is  $1 \text{ m s}^{-1}$ .

the critical level (not shown). As time progresses, the low-level weak downward motion also appears for high- $\text{Ri}$  flow with shallow heating (Fig. 7a). The strongest downward motion is produced for low- $\text{Ri}$  flow with a heating top located a little below the critical level ( $z = 4.6 \text{ km}$ ). On the other hand, in three dimensions where a low-level downward motion induced by reflected gravity waves is generally weaker than that in two dimensions, there is always a low-level upward motion at the heating center regardless of the values of  $\text{Ri}$  and the heating depth (Fig. 7b). A low-level upward motion of the strongest intensity occurs for high- $\text{Ri}$  flow with a heating top located around  $z = 3$  and  $2.7 \text{ km}$  in two and three dimensions, respectively.

Note that for deep heating across a critical level, there exists a low-level upward motion at the heating center at all times in both two and three dimensions for all the values of  $\text{Ri}$  and the heating depth considered. After some time, the magnitude of the low-level upward motion changes little, although the heating top height increases.

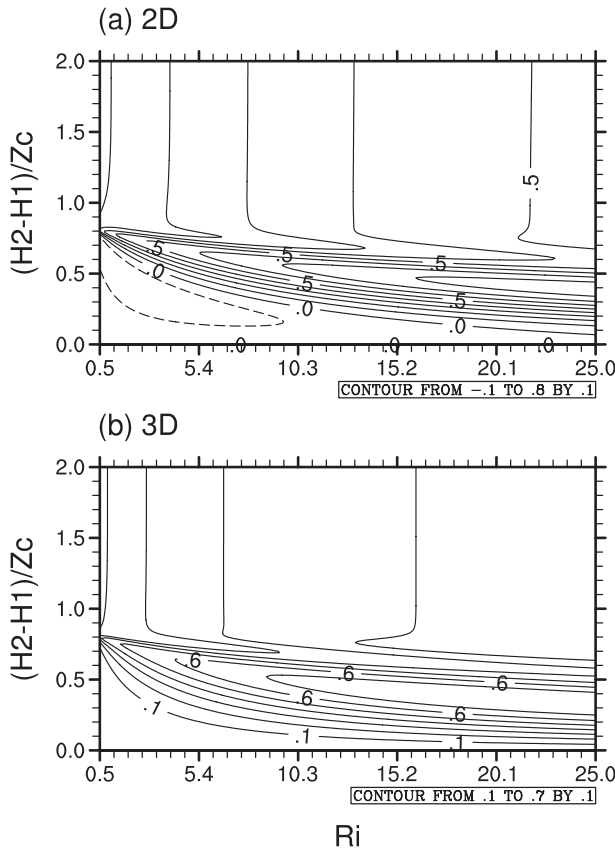


FIG. 7. The perturbation vertical velocity at the heating center ( $x = 0$  km) and heating bottom height ( $z = 1$  km) at  $t = 2$  h as a function of Richardson number ( $Ri = N^2/\alpha^2$ ) and the heating depth nondimensionalized by the critical level height  $[(h_2 - h_1)/z_c]$  in (a) two and (b) three (at  $y = 0$  km) dimensions. The contour interval is  $0.1 \text{ m s}^{-1}$ .

This can be explained as follows: For nonzero values of  $t$  and  $\cos\theta$ ,  $U_h$  and  $\theta_h\mu'$  {where  $\theta_h = \arctan(U_h t \cos\theta/\alpha)$  at the heating center and  $\mu' = \text{sgn}(\cos\theta)[(Ri/\cos^2\theta) - 1/4]^{1/2}$ } are positive and negative for heating applied below and above the critical level, respectively, and their magnitudes increase for heating away from the critical level. Accordingly, at a certain height below the critical level (say,  $z = z_b$ ),  $(\theta_h - \theta_z)\mu'$  for heating applied above  $z = z_b$  is negative and its magnitude increases as the heating is located farther above  $z = z_b$ . Therefore, the magnitude of the attenuation factor for downward-propagating gravity waves  $[e^{(\theta_h - \theta_z)\mu'}]$  in (A5a)] at  $z = z_b$  decreases when waves are induced by the heating located farther above  $z = z_b$  and becomes particularly small for heating applied a little above the critical level where  $\theta_h\mu'$  changes its sign from positive to negative. This is shown in Fig. 8, where  $e^{(\theta_h - \theta_z)\mu'}$  at  $z = 1$  km is plotted as a function of the height where the forcing is applied. Downward-propagating gravity waves induced by the

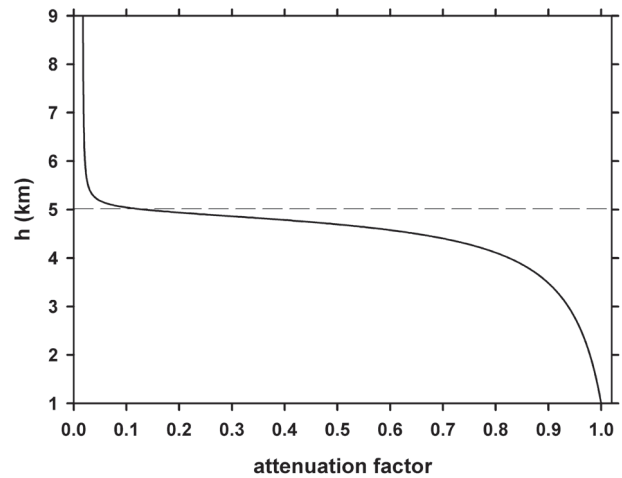


FIG. 8. The attenuation factor for downward-propagating gravity waves  $[e^{(\theta_h - \theta_z)\mu'}]$  in (A5a)] with the parameter values of  $\cos\theta = 1$  and  $Ri = 2$  at the heating center ( $x = y = 0$  km) and  $z = 1$  km at  $t = 2$  h as a function of the height where the forcing is applied ( $h$ ).

heat source above, but not near, the critical level are almost absorbed at the critical level and therefore have little effect on the flow response field below the critical level. As a result, there is almost no change in the perturbation field below the critical level, although the heating top height increases.

Next, we examine the effects of varying basic-state wind direction with height on convectively forced flows. In a unidirectional shear flow, the critical level for all gravity waves with zero horizontal phase speeds is the level of zero basic-state wind speed. In a directional shear flow, however, each gravity wave with zero horizontal phase speed has a different critical level satisfying  $Uk + Vl = 0$  (Shutts and Gadian 1999). Therefore, some gravity waves with zero horizontal phase speeds, whose wave vector is not perpendicular to the basic-state wind direction at any height, cannot experience the critical-level effect. From the result that the steady-state vertical flux of horizontal momentum is not height-independent in a directional shear flow because of selective critical-level absorption (Shutts 1995), Vosper and Mobbs (1998) suggested that when the basic-state flow exhibits turning with height, the steady-state assumption is not valid.

Figure 9 shows the perturbation vertical velocity fields at various heights at  $t = 2$  h in a constant directional shear flow. The specified parameter values are the same as those in the case of a constant unidirectional shear flow with finite-depth steady heating except for  $V_0 = 10 \text{ m s}^{-1}$ . The basic-state wind backs with height. The overall pattern of the vertical velocity field bears resemblance to that in a constant unidirectional shear flow, but there are some differences. As in a constant

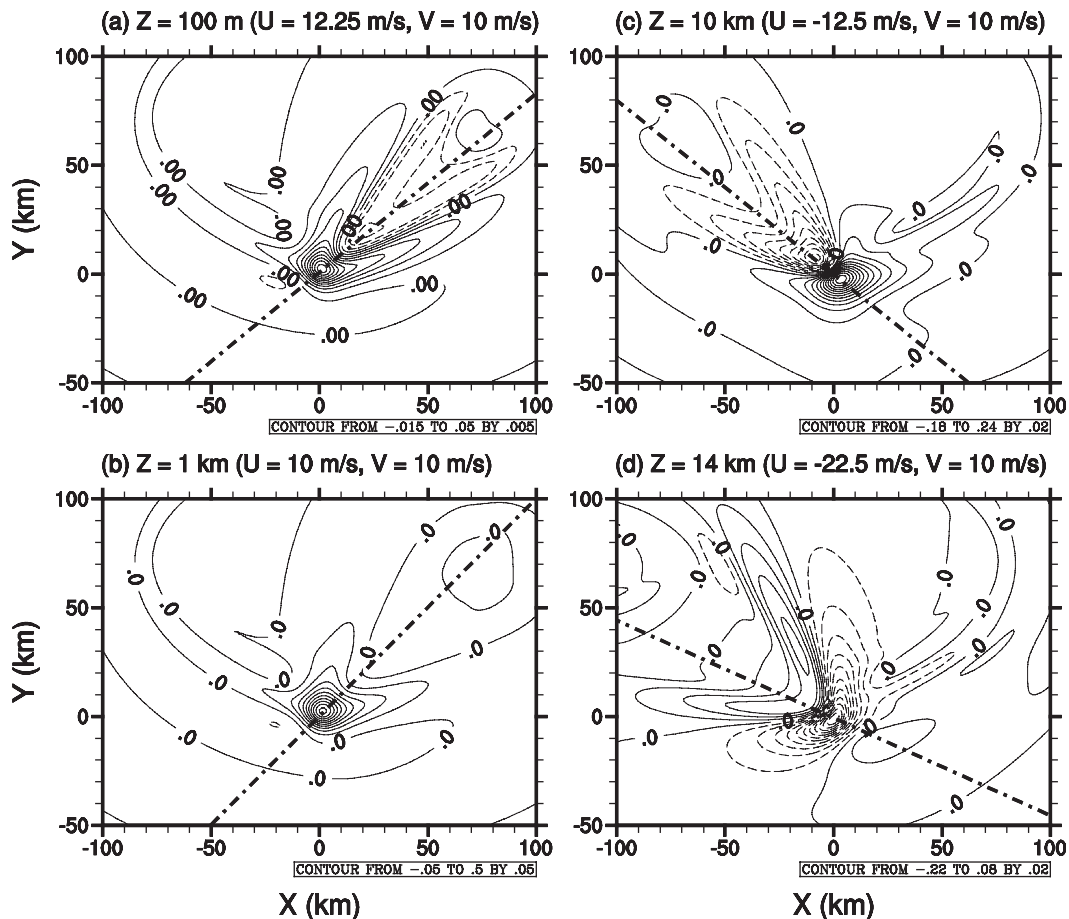


FIG. 9. The perturbation vertical velocity fields at heights of  $z =$  (a) 100 m, (b) 1 km, (c) 10 km, and (d) 14 km at  $t = 2$  h in a constant directional shear flow with finite-depth steady heating applied uniformly in the vertical from  $z = 1$  to 9 km. The specified parameter values are the same as those in the case of a constant unidirectional shear flow with finite-depth steady heating except for  $V_0 = 10 \text{ m s}^{-1}$ . The basic-state wind direction passing through the heating center is indicated by the dashed-dotted line in each figure. The contour intervals are  $0.005 \text{ m s}^{-1}$  in (a),  $0.05 \text{ m s}^{-1}$  in (b), and  $0.02 \text{ m s}^{-1}$  in (c) and (d).

unidirectional shear flow, the flow response field exhibits V-shaped upward and downward motions above and below the steady heating layer. However, they are no longer symmetric about the basic-state wind direction passing through the heating center (dashed-dotted line in Fig. 9), and the vertices of V-shaped features above and below the heating layer point to directions rotated a little clockwise and counterclockwise from the basic-state wind direction, respectively (Figs. 9a,c,d). This is because at a certain height above (below) the heating layer, the V-shaped feature is produced by direct upward-propagating (downward-propagating) gravity waves that have passed through the layer below (above) where the basic-state wind direction is clockwise (counterclockwise) relative to that above (below). On the other hand, near the heating bottom where the V-shaped feature is mainly produced by reflected gravity waves that have

passed through the layer below the heating bottom, the vertex points to a direction rotated a little clockwise from the basic-state wind direction (Fig. 9b). The angle between the basic-state wind direction and the direction the vertex points increases away from the steady heating layer (Figs. 9c,d).

Figure 10 shows the vertical variations of the vertical flux of the zonal and meridional momentum integrated over the horizontal plane at  $t = 1800 \text{ s}$ , 1 h, and 2 h in a constant directional shear flow. At early times, the zonal momentum flux in a directional shear flow shows a vertical variation similar to that in a unidirectional shear flow (dotted lines in Figs. 5 and 10a). In a directional shear flow, however, a weaker positive  $x$ -directional perturbation velocity in the steady heating layer causes a smaller magnitude of the zonal momentum flux there. As time progresses, regions of negative  $x$ -directional

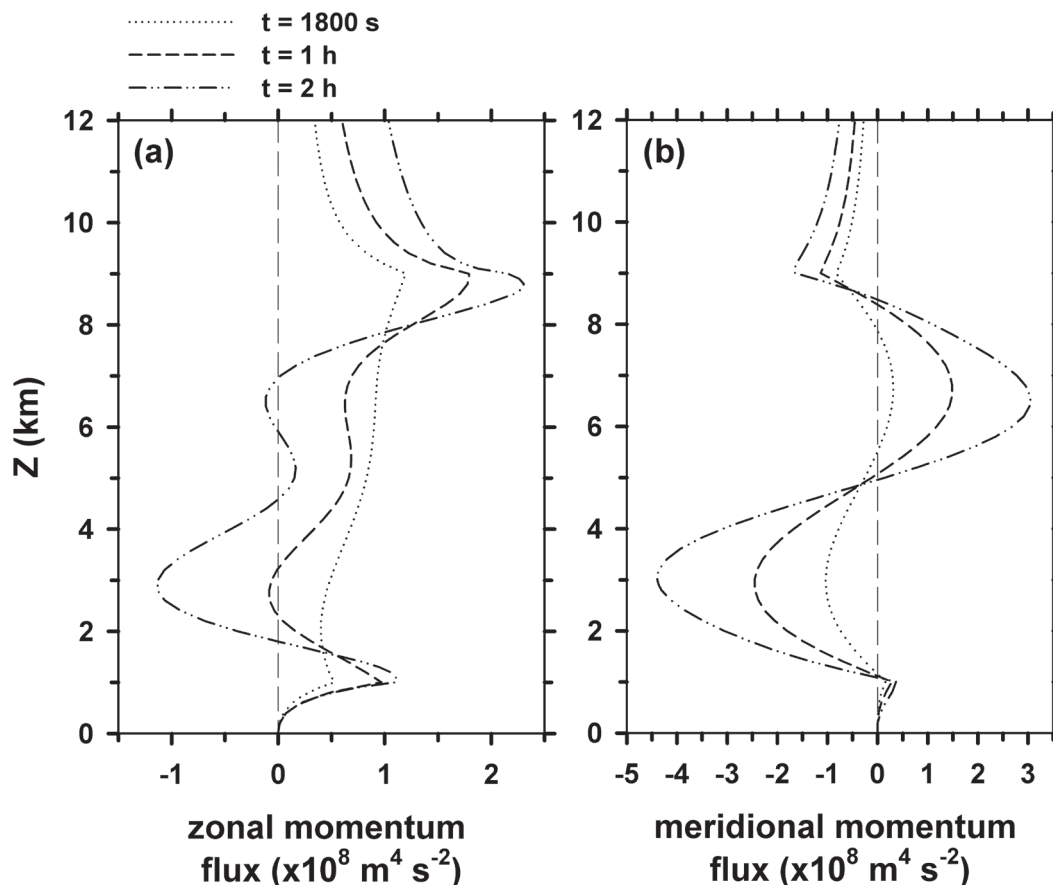


FIG. 10. The vertical variations of the vertical flux of the (a) zonal and (b) meridional momentum integrated over the horizontal plane ( $\text{m}^4 \text{ s}^{-2}$ ) at  $t = 1800 \text{ s}$ ,  $1 \text{ h}$ , and  $2 \text{ h}$  in a constant directional shear flow with finite-depth steady heating applied uniformly in the vertical from  $z = 1$  to  $9 \text{ km}$ .

perturbation velocity are located in the steady heating layer, resulting in a negative momentum flux in large parts of the steady heating layer (dashed–double dotted line in Fig. 10a). On the other hand, the vertical profile of the meridional momentum flux in a directional shear flow exhibits a time evolution similar to the vertical profile of the zonal momentum flux in a uniform flow, but the magnitudes of the momentum flux near the heating bottom and top are smaller than those in a uniform flow (compare Fig. 5 of Part I with Fig. 10b). The layers of both zonal and meridional mean flow decelerations, which can arise from the vertical convergence/divergence of the momentum flux, are observed below and above the heating layer and in large parts of the middle region of the heating layer.

#### 4. Summary and conclusions

In Part I of this study, we studied some linear dynamics of convectively forced mesoscale flows by solving

a 3D transient problem in a uniform flow with diabatic forcing analytically. Here, we solved a 3D transient problem in a shear flow with a critical level to further study convectively forced mesoscale flows.

In a unidirectional shear flow with surface pulse heating, the magnitude of perturbations in the region where gravity waves do not pass through the transient critical level is relatively large even far from the heating because the vertical wind shear acts as an additional source of wave energy. The magnitude of the maximum upward motion observed at the center of the moving mode becomes constant after some time, whereas the magnitudes of the vertical displacement and perturbation horizontal velocity near the center of the moving mode increase linearly with time. This finding is valid regardless of whether or not the basic-state wind is uniform with height and whether the airflow system considered is 2D or 3D.

In a unidirectional shear flow with finite-depth steady heating that is considered to represent latent heat

release in deep cumulus convection, the layers of mean flow deceleration, which can result from the vertical convergence/divergence of the momentum flux, appear below, above, and in the middle region of the heating layer as in a uniform flow. In three dimensions, there always exists a low-level upward motion at the heating center no matter what the intensity of vertical wind shear and the heating depth are. For heating located across a critical level, the magnitude of a low-level upward motion at the heating center changes little, even if the heating top height increases. This is because downward-propagating gravity waves that come directly from the heating above, but not near, the critical level have almost no influence on the perturbation field below the critical level. In a directional shear flow with a backing of the basic-state wind with height, the vertex of V-shaped upward or downward motion above the heating top points to a direction rotated a little clockwise from the basic-state wind direction. This is because the V-shaped feature above the heating top is generated by the action of upward-propagating gravity waves that have passed through the layer below where the basic-state wind direction is clockwise relative to that above.

In this study, we mainly investigated the effects of vertical wind shear and critical level on convective heating-induced circulation. However, more applications of the solutions to some complex thermally forced mesoscale phenomena can be considered. One of them is the flow response field to squall-line type forcing. By performing a two-dimensional numerical simulation of a squall line, Pandya and Durran (1996) indicated that most of the interior of the leading convective line–trailing anvil system is stably stratified and therefore gravity waves can propagate throughout essentially the entire system. They also showed that much of the mesoscale structure associated with squall lines is determined by gravity waves forced by thermal forcing in

and near the leading convective line. Thus, we would be able to understand more basic linear dynamics of squall-line systems from our 3D transient solutions if more realistic environmental conditions and forcing structures were considered. In this study, we assumed that the flow is in hydrostatic balance. In the case of orographically generated gravity waves, it was found that for strongly sheared flow the hydrostatic approximation may not be justified for gravity wave calculations even for a relatively large horizontal size of forcing (Keller 1994). Thus, it would be worthwhile investigating the extent to which the hydrostatic assumption is valid for thermally generated gravity waves in a shear flow. In this study, we also assumed a nonrotating flow. Despite some influence of the Coriolis force on the evolution of convectively forced mesoscale flows, not many of theoretical studies considered a rotating flow because of mathematical difficulty. In a future work, a theoretical examination of Coriolis effects on convectively forced mesoscale flows is needed.

*Acknowledgments.* The authors are very grateful to two anonymous reviewers for providing valuable comments on this work. This work was funded by the Korea Meteorological Administration Research and Development Program under Grant CATER 2006-2202 and the Brain Korea 21 Project.

## APPENDIX

### Solutions for the Perturbation Vertical Velocity in Physical Space

We divide (12a) by  $(ik)^2$  to simplify calculations and then apply the inverse Laplace transform in  $s$  ( $\rightarrow t$ ) and the inverse double Fourier transform in  $k$  ( $\rightarrow x$ ) and  $l$  ( $\rightarrow y$ ):

$$\begin{aligned}
 & \int_0^x \int_0^x w_1(x, y, z, t) dx dx + \int_{-\infty}^{\infty} \mathcal{L}^{-1}[W_1(0, y, z, t)x + W_2(0, y, z, t)]e^{ily} dl \\
 &= \text{Re} \left[ C_1 \int_{-\infty}^{\infty} \int_{-\infty}^{\infty} \int_0^t \frac{1}{(ik)^2} \frac{(ik)^2 + (il)^2}{(2i\mu')(ik\alpha + il\beta)} e^{-\sqrt{k^2 a_x^2 + l^2 a_y^2}} \right. \\
 & \quad \times \frac{(t - \sigma)^{1/2 + i\mu'} \sigma^{-3/2 - i\mu'}}{\Gamma(3/2 + i\mu')\Gamma(-1/2 - i\mu')} e^{-(ikU_h + ilV_h)(t - \sigma)} e^{-(ikU + ilV)\sigma} e^{ikx} e^{ily} d\sigma dk dl \\
 & \quad - C_1 \int_{-\infty}^{\infty} \int_{-\infty}^{\infty} \int_0^t \int_0^{\tau} \frac{1}{(ik)^2} \frac{(ik)^2 + (il)^2}{(2i\mu')(ik\alpha + il\beta)} e^{-\sqrt{k^2 a_x^2 + l^2 a_y^2}} \\
 & \quad \times \frac{(t - \tau)^{1/2 + i\mu'} (\tau - \sigma)^{-1 - 2i\mu'} \sigma^{-3/2 + i\mu'}}{\Gamma(3/2 + i\mu')\Gamma(-2i\mu')\Gamma(-1/2 + i\mu')} e^{-(ikU_0 + ilV_0)(\tau - \sigma)} e^{-(ikU + ilV)\sigma} e^{-(ikU_h + ilV_h)(t - \tau)} e^{ikx} e^{ily} d\sigma d\tau dk dl \left. \right], \quad (\text{A1})
 \end{aligned}$$



where a formula of  $\mathcal{F}^{-1}[\hat{w}_1(k)/(ik)^2] = \int_0^x \int_0^x w_1(x) dx dx + [W_1(0)x + W_2(0)]$  is used. Here,  $\mathcal{F}^{-1}$  and  $\mathcal{L}^{-1}$  are the inverse Fourier and Laplace transform operators, respectively,  $W_1(x, y, z, t) = \int w_1 dx$ ,  $W_2(x, y, z, t) = \int \int w_1 dx dx$ ,

and  $\Gamma$  is the gamma function. Converting (A1) into an integral in polar coordinates and integrating with respect to  $K$  yields

$$\begin{aligned} & \int_0^x \int_0^x w_1(x, y, z, t) dx dx + \int_{-\infty}^{\infty} \mathcal{L}^{-1}[W_1(0, y, z, t)x + W_2(0, y, z, t)]e^{ily} dl \\ &= \text{Re} \left[ \int_0^{2\pi} \frac{C_\theta}{\Gamma(3/2 + i\mu')\Gamma(-1/2 - i\mu') \cos^2\theta} \int_0^t (t - \sigma)^{1/2+i\mu'} \sigma^{-3/2-i\mu'} \frac{1}{T} d\sigma d\theta \right. \\ & \quad \left. - \int_0^{2\pi} \frac{C_\theta}{\Gamma(3/2 + i\mu')\Gamma(-2i\mu')\Gamma(-1/2 + i\mu') \cos^2\theta} \int_0^t (t - \tau)^{1/2+i\mu'} \int_0^\tau (\tau - \sigma)^{-1-2i\mu'} \sigma^{-3/2+i\mu'} \frac{1}{T'} d\sigma d\tau d\theta \right], \quad (\text{A2}) \end{aligned}$$

where

$$K = \sqrt{k^2 + l^2}, \quad C_\theta = -\frac{gq_0 a_x a_y}{4\pi c_p T_0 \mu'} \frac{1}{(\alpha \cos\theta + \beta \sin\theta)},$$

$$\theta = \arctan\left(\frac{l}{k}\right),$$

$$\begin{aligned} T &= a + i\{[U_h t + (U - U_h)\sigma - x] \cos\theta \\ & \quad + [V_h t + (V - V_h)\sigma - y] \sin\theta\}, \end{aligned}$$

$$\begin{aligned} T' &= a + i\{[U_h t + (U_0 - U_h)\tau + (U - U_0)\sigma - x] \cos\theta \\ & \quad + [V_h t + (V_0 - V_h)\tau + (V - V_0)\sigma - y] \sin\theta\}, \end{aligned}$$

$$a = a_x \sqrt{\cos^2\theta + \gamma^2 \sin^2\theta}, \quad \gamma = \frac{a_y}{a_x}.$$

After integration with respect to  $\sigma$  and  $\tau$ , (A2) becomes

$$\begin{aligned} & \int_0^x \int_0^x w_1(x, y, z, t) dx dx + \int_{-\infty}^{\infty} \mathcal{L}^{-1}[W_1(0, y, z, t)x + W_2(0, y, z, t)]e^{ily} dl \\ &= \text{Re} \left[ \int_0^{2\pi} \frac{C_\theta}{\cos^2\theta} (B_h^{-3/2-i\mu'} B_z^{1/2+i\mu'} - B_h^{-3/2-i\mu'} B_0^{2i\mu'} B_z^{1/2-i\mu'}) d\theta \right], \quad (\text{A3}) \end{aligned}$$

where

$$B_h = a + i[(U_h t - x) \cos\theta + (V_h t - y) \sin\theta],$$

$$B_0 = a + i[(U_0 t - x) \cos\theta + (V_0 t - y) \sin\theta],$$

$$B_z = a + i[(Ut - x) \cos\theta + (Vt - y) \sin\theta].$$

Finally, differentiating (A3) twice with respect to  $x$  leads to the solution for the perturbation vertical velocity to the surface pulse forcing for  $0 \leq z \leq h$ :

$$\begin{aligned} w_1(x, y, z, t) &= \text{Re} \left\{ \int_0^{2\pi} C_\theta \left[ -\left(\frac{5}{2} + i\mu'\right) \left(\frac{3}{2} + i\mu'\right) B_h^{-7/2-i\mu'} B_z^{1/2+i\mu'} + 2 \left(\frac{3}{2} + i\mu'\right) \left(\frac{1}{2} + i\mu'\right) B_h^{-5/2-i\mu'} B_z^{-1/2+i\mu'} \right. \right. \\ & \quad \left. \left. - \left(\frac{1}{2} + i\mu'\right) \left(-\frac{1}{2} + i\mu'\right) B_h^{-3/2-i\mu'} B_z^{-3/2+i\mu'} \right] d\theta \right\} + \text{REF}_{sp}, \quad (\text{A4a}) \end{aligned}$$

where

$$\begin{aligned} \text{REF}_{sp} &= \text{Re} \left\{ \int_0^{2\pi} C_\theta \left[ \left(\frac{5}{2} + i\mu'\right) \left(\frac{3}{2} + i\mu'\right) B_h^{-7/2-i\mu'} B_0^{2i\mu'} B_z^{1/2-i\mu'} - 2 \left(\frac{3}{2} + i\mu'\right) (2i\mu') B_h^{-5/2-i\mu'} B_0^{-1+2i\mu'} B_z^{1/2-i\mu'} \right. \right. \\ & \quad - 2 \left(\frac{3}{2} + i\mu'\right) \left(\frac{1}{2} - i\mu'\right) B_h^{-5/2-i\mu'} B_0^{2i\mu'} B_z^{-1/2-i\mu'} + (-1 + 2i\mu')(2i\mu') B_h^{-3/2-i\mu'} B_0^{-2+2i\mu'} B_z^{1/2-i\mu'} \\ & \quad \left. \left. + 2 \left(\frac{1}{2} - i\mu'\right) (2i\mu') B_h^{-3/2-i\mu'} B_0^{-1+2i\mu'} B_z^{-1/2-i\mu'} - \left(\frac{1}{2} + i\mu'\right) \left(\frac{1}{2} - i\mu'\right) B_h^{-3/2-i\mu'} B_0^{2i\mu'} B_z^{-3/2-i\mu'} \right] d\theta \right\}. \end{aligned}$$

In a similar way, it can be shown that the solution for  $z > h$  is

$$w_2(x, y, z, t) = \text{Re} \left\{ \int_0^{2\pi} C_\theta \left[ -\left(\frac{5}{2} - i\mu'\right) \left(\frac{3}{2} - i\mu'\right) B_h^{-7/2+i\mu'} B_z^{1/2-i\mu'} + 2\left(\frac{3}{2} - i\mu'\right) \left(\frac{1}{2} - i\mu'\right) B_h^{-5/2+i\mu'} B_z^{-1/2-i\mu'} \right. \right. \\ \left. \left. - \left(\frac{1}{2} - i\mu'\right) \left(-\frac{1}{2} - i\mu'\right) B_h^{-3/2+i\mu'} B_z^{-3/2-i\mu'} \right] d\theta \right\} + \text{REF}_{sp}. \quad (\text{A4b})$$

Here, REF is the part of the solution that represents upward-propagating gravity waves resulted from re-

flection at the bottom boundary and the subscript  $sp$  indicates the surface pulse forcing.

Evaluating the real part of (A5) gives

$$w_1(x, y, z, t) = \int_0^{2\pi} C_\theta e^{(\theta_h - \theta_z)\mu'} \left\{ R_h^{-7/2} R_z^{1/2} \left[ \left(-\frac{15}{4} + \mu'^2\right) \cos f_1 - 4\mu' \sin f_1 \right] + R_h^{-5/2} R_z^{-1/2} \left[ \left(\frac{3}{2} - 2\mu'^2\right) \cos f_2 \right. \right. \\ \left. \left. + 4\mu' \sin f_2 \right] + R_h^{-3/2} R_z^{-3/2} \left(\frac{1}{4} + \mu'^2\right) \cos f_3 \right\} d\theta + \text{REF}'_{sp} \quad \text{for } 0 \leq z \leq h, \quad (\text{A5a})$$

$$w_2(x, y, z, t) = \int_0^{2\pi} C_\theta e^{(-\theta_h + \theta_z)\mu'} \left\{ R_h^{-7/2} R_z^{1/2} \left[ \left(-\frac{15}{4} + \mu'^2\right) \cos f_{10} + 4\mu' \sin f_{10} \right] + R_h^{-5/2} R_z^{-1/2} \left[ \left(\frac{3}{2} - 2\mu'^2\right) \cos f_{11} \right. \right. \\ \left. \left. - 4\mu' \sin f_{11} \right] + R_h^{-3/2} R_z^{-3/2} \left(\frac{1}{4} + \mu'^2\right) \cos f_{12} \right\} d\theta + \text{REF}'_{sp} \quad \text{for } z > h, \quad (\text{A5b})$$

where

$$\text{REF}'_{sp} = \int_0^{2\pi} C_\theta e^{(\theta_h - 2\theta_0 + \theta_z)\mu'} \left\{ R_h^{-7/2} R_z^{1/2} \left[ \left(\frac{15}{4} - \mu'^2\right) \cos f_4 + 4\mu' \sin f_4 \right] + R_h^{-5/2} R_0^{-1} R_z^{1/2} (4\mu'^2 \cos f_5 - 6\mu' \sin f_5) \right. \\ \left. + R_h^{-5/2} R_z^{-1/2} \left[ \left(-\frac{3}{2} - 2\mu'^2\right) \cos f_6 + 2\mu' \sin f_6 \right] + R_h^{-3/2} R_0^{-1} R_z^{-1/2} (4\mu'^2 \cos f_7 + 2\mu' \sin f_7) \right. \\ \left. + R_h^{-3/2} R_0^{-2} R_z^{1/2} (-4\mu'^2 \cos f_8 - 2\mu' \sin f_8) + R_h^{-3/2} R_z^{-3/2} \left(-\frac{1}{4} - \mu'^2\right) \cos f_9 \right\} d\theta,$$

$$R_h = \sqrt{a^2 + [(U_h t - x) \cos \theta + (V_h t - y) \sin \theta]^2},$$

$$\theta_h = \arctan \frac{(U_h t - x) \cos \theta + (V_h t - y) \sin \theta}{a},$$

$$R_z = \sqrt{a^2 + [(U t - x) \cos \theta + (V t - y) \sin \theta]^2},$$

$$\theta_z = \arctan \frac{(U t - x) \cos \theta + (V t - y) \sin \theta}{a},$$

$$R_0 = \sqrt{a^2 + [(U_0 t - x) \cos \theta + (V_0 t - y) \sin \theta]^2},$$

$$\theta_0 = \arctan \frac{(U_0 t - x) \cos \theta + (V_0 t - y) \sin \theta}{a},$$

$$f_1 = \frac{7}{2} \theta_h - \frac{1}{2} \theta_z + \mu' \ln \left( \frac{R_h}{R_z} \right),$$

$$f_2 = \frac{5}{2} \theta_h + \frac{1}{2} \theta_z + \mu' \ln \left( \frac{R_h}{R_z} \right),$$

$$f_3 = \frac{3}{2} \theta_h + \frac{3}{2} \theta_z + \mu' \ln \left( \frac{R_h}{R_z} \right),$$

$$f_4 = \frac{7}{2} \theta_h - \frac{1}{2} \theta_z + \mu' \ln \left( \frac{R_h R_z}{R_0^2} \right),$$

$$f_5 = \frac{5}{2} \theta_h + \theta_0 - \frac{1}{2} \theta_z + \mu' \ln \left( \frac{R_h R_z}{R_0^2} \right),$$

$$f_6 = \frac{5}{2} \theta_h + \frac{1}{2} \theta_z + \mu' \ln \left( \frac{R_h R_z}{R_0^2} \right),$$

$$f_7 = \frac{3}{2} \theta_h + \theta_0 + \frac{1}{2} \theta_z + \mu' \ln \left( \frac{R_h R_z}{R_0^2} \right),$$

$$f_8 = \frac{3}{2} \theta_h + 2\theta_0 - \frac{1}{2} \theta_z + \mu' \ln \left( \frac{R_h R_z}{R_0^2} \right),$$

$$f_9 = \frac{3}{2}\theta_h + \frac{3}{2}\theta_z + \mu' \ln\left(\frac{R_h R_z}{R_0^2}\right),$$

$$f_{10} = \frac{7}{2}\theta_h - \frac{1}{2}\theta_z - \mu' \ln\left(\frac{R_h}{R_z}\right),$$

$$f_{11} = \frac{5}{2}\theta_h + \frac{1}{2}\theta_z - \mu' \ln\left(\frac{R_h}{R_z}\right),$$

$$f_{12} = \frac{3}{2}\theta_h + \frac{3}{2}\theta_z - \mu' \ln\left(\frac{R_h}{R_z}\right).$$

Here, the attenuation factors for downward-propagating and upward-propagating gravity waves that come directly from the thermal forcing are  $e^{(\theta_h - \theta_z)\mu'}$  in (A5a) and  $e^{(-\theta_h + \theta_z)\mu'}$  in (A5b), respectively, and the attenuation factor for upward-propagating gravity waves that are reflected from the bottom boundary is  $e^{(\theta_h - 2\theta_0 + \theta_z)\mu'}$  in  $\text{REF}'_{sp}$ .

The solution for the perturbation vertical velocity to the finite-depth steady forcing distributed uniformly in the vertical from  $z = h_1$  to  $h_2$  is obtained by integrating (A4) with respect to forcing level and time:

$$w_1(x, y, z, t) = \text{Re} \left\{ \int_0^{2\pi} \frac{C'_\theta}{B} \left[ B_z^{1/2+i\mu'} (B_2^{-3/2-i\mu'} - B_1^{-3/2-i\mu'}) - B_z^{-1/2+i\mu'} (B_2^{-1/2-i\mu'} - B_1^{-1/2-i\mu'}) \right. \right. \\ \left. \left. + \frac{1}{(1/2+i\mu')B} B_z^{1/2+i\mu'} (B_2^{-1/2-i\mu'} - B_1^{-1/2-i\mu'}) \right] d\theta \right\} + \text{REF}_{fs} \quad \text{for } 0 \leq z \leq h_1, \quad (\text{A6a})$$

$$w_2(x, y, z, t) = \text{Re} \left\{ \int_0^{2\pi} \frac{C'_\theta}{B} \left[ B_z^{1/2-i\mu'} (B_2^{-3/2+i\mu'} - B_1^{-3/2+i\mu'}) - B_z^{-1/2-i\mu'} (B_2^{-1/2+i\mu'} - B_1^{-1/2+i\mu'}) \right. \right. \\ \left. \left. + \frac{1}{(1/2-i\mu')B} B_z^{1/2-i\mu'} (B_2^{-1/2+i\mu'} - B_1^{-1/2+i\mu'}) + B_z^{1/2+i\mu'} (B_2^{-3/2-i\mu'} - B_z^{-3/2-i\mu'}) \right. \right. \\ \left. \left. - B_z^{-1/2+i\mu'} (B_2^{-1/2-i\mu'} - B_z^{-1/2-i\mu'}) + \frac{1}{(1/2+i\mu')B} B_z^{1/2+i\mu'} (B_2^{-1/2-i\mu'} - B_z^{-1/2-i\mu'}) \right] d\theta \right\} \\ + \text{REF}_{fs} \quad \text{for } h_1 < z \leq h_2, \quad (\text{A6b})$$

$$w_3(x, y, z, t) = \text{Re} \left\{ \int_0^{2\pi} \frac{C'_\theta}{B} \left[ B_z^{1/2-i\mu'} (B_2^{-3/2+i\mu'} - B_1^{-3/2+i\mu'}) - B_z^{-1/2-i\mu'} (B_2^{-1/2+i\mu'} - B_1^{-1/2+i\mu'}) \right. \right. \\ \left. \left. + \frac{1}{(1/2-i\mu')B} B_z^{1/2-i\mu'} (B_2^{-1/2+i\mu'} - B_1^{-1/2+i\mu'}) \right] d\theta \right\} + \text{REF}_{fs} \quad \text{for } z > h_2, \quad (\text{A6c})$$

where

$$\text{REF}_{fs} = \text{Re} \left\{ \int_0^{2\pi} \frac{C'_\theta}{B} \left[ -B_0^{2i\mu'} B_z^{1/2-i\mu'} (B_2^{-3/2-i\mu'} - B_1^{-3/2-i\mu'}) + \frac{2i\mu'}{1/2+i\mu'} B_0^{-1+2i\mu'} B_z^{1/2-i\mu'} (B_2^{-1/2-i\mu'} - B_1^{-1/2-i\mu'}) \right. \right. \\ \left. \left. + \frac{1/2-i\mu'}{1/2+i\mu'} B_0^{2i\mu'} B_z^{-1/2-i\mu'} (B_2^{-1/2-i\mu'} - B_1^{-1/2-i\mu'}) - \frac{1}{(1/2+i\mu')B} B_0^{2i\mu'} B_z^{1/2-i\mu'} (B_2^{-1/2-i\mu'} - B_1^{-1/2-i\mu'}) \right] d\theta \right\},$$

$$C'_\theta = \frac{gq_0 a_x a_y}{4\pi c_p T_0 \mu'} \frac{1}{i(\alpha \cos\theta + \beta \sin\theta)^2},$$

$$B = a - i(x \cos\theta + y \sin\theta),$$

$$B_1 = a + i[(U_1 t - x) \cos\theta + (V_1 t - y) \sin\theta],$$

$$U_1 = U_0 - \alpha h_1,$$

$$V_1 = V_0 - \beta h_1,$$

$$B_2 = a + i[(U_2 t - x) \cos\theta + (V_2 t - y) \sin\theta],$$

$$U_2 = U_0 - \alpha h_2,$$

$$V_2 = V_0 - \beta h_2.$$

Here, the subscript  $fs$  indicates the finite-depth steady forcing.

Evaluating the real part of (A6) gives

$$\begin{aligned}
w_1(x, y, z, t) = & \int_0^{2\pi} \frac{iC'_\theta}{a^2 + X_Y^2} \left\{ -R_2^{-3/2} R_z^{1/2} e^{(\theta_2 - \theta_z)\mu'} (a \sin q_1 - X_Y \cos q_1) \right. \\
& + R_1^{-3/2} R_z^{1/2} e^{(\theta_1 - \theta_z)\mu'} (a \sin q'_1 - X_Y \cos q'_1) \\
& + R_2^{-1/2} R_z^{-1/2} e^{(\theta_2 - \theta_z)\mu'} (a \sin q_2 - X_Y \cos q_2) - R_1^{-1/2} R_z^{-1/2} e^{(\theta_1 - \theta_z)\mu'} (a \sin q'_2 - X_Y \cos q'_2) \\
& - \frac{R_2^{-1/2} R_z^{1/2} e^{(\theta_2 - \theta_z)\mu'}}{(1/4 + \mu'^2)(a^2 + X_Y^2)} \left[ \left( \frac{1}{2} a^2 - \frac{1}{2} X_Y^2 + 2aX_Y \mu' \right) \sin q_3 - (aX_Y - a^2 \mu' + X_Y^2 \mu') \cos q_3 \right] \\
& + \frac{R_1^{-1/2} R_z^{1/2} e^{(\theta_1 - \theta_z)\mu'}}{(1/4 + \mu'^2)(a^2 + X_Y^2)} \left[ \left( \frac{1}{2} a^2 - \frac{1}{2} X_Y^2 + 2aX_Y \mu' \right) \sin q'_3 - (aX_Y - a^2 \mu' + X_Y^2 \mu') \cos q'_3 \right] \Big\} d\theta \\
& + \text{REF}'_{fs} \quad \text{for } 0 \leq z \leq h_1,
\end{aligned} \tag{A7a}$$

$$\begin{aligned}
w_2(x, y, z, t) = & \int_0^{2\pi} \frac{iC'_\theta}{a^2 + X_Y^2} \left\{ R_1^{-3/2} R_z^{1/2} e^{(-\theta_1 + \theta_z)\mu'} (a \sin q'_8 - X_Y \cos q'_8) \right. \\
& - R_1^{-1/2} R_z^{-1/2} e^{(-\theta_1 + \theta_z)\mu'} (a \sin q'_9 - X_Y \cos q'_9) \\
& - R_2^{-3/2} R_z^{1/2} e^{(\theta_2 - \theta_z)\mu'} (a \sin q_1 - X_Y \cos q_1) + R_2^{-1/2} R_z^{-1/2} e^{(\theta_2 - \theta_z)\mu'} (a \sin q_2 - X_Y \cos q_2) \\
& + \frac{R_1^{-1/2} R_z^{1/2} e^{(-\theta_1 + \theta_z)\mu'}}{(1/4 + \mu'^2)(a^2 + X_Y^2)} \left[ \left( \frac{1}{2} a^2 - \frac{1}{2} X_Y^2 - 2aX_Y \mu' \right) \sin q'_{10} - (aX_Y + a^2 \mu' - X_Y^2 \mu') \cos q'_{10} \right] \\
& - \frac{R_2^{-1/2} R_z^{1/2} e^{(\theta_2 - \theta_z)\mu'}}{(1/4 + \mu'^2)(a^2 + X_Y^2)} \left[ \left( \frac{1}{2} a^2 - \frac{1}{2} X_Y^2 + 2aX_Y \mu' \right) \sin q_3 - (aX_Y - a^2 \mu' + X_Y^2 \mu') \cos q_3 \right] \Big\} d\theta \\
& + \text{REF}'_{fs} \quad \text{for } h_1 < z \leq h_2,
\end{aligned} \tag{A7b}$$

$$\begin{aligned}
w_3(x, y, z, t) = & \int_0^{2\pi} \frac{iC'_\theta}{a^2 + X_Y^2} \left\{ -R_2^{-3/2} R_z^{1/2} e^{(-\theta_2 + \theta_z)\mu'} (a \sin q_8 - X_Y \cos q_8) \right. \\
& + R_1^{-3/2} R_z^{1/2} e^{(-\theta_1 + \theta_z)\mu'} (a \sin q'_8 - X_Y \cos q'_8) \\
& + R_2^{-1/2} R_z^{-1/2} e^{(-\theta_2 + \theta_z)\mu'} (a \sin q_9 - X_Y \cos q_9) - R_1^{-1/2} R_z^{-1/2} e^{(-\theta_1 + \theta_z)\mu'} (a \sin q'_9 - X_Y \cos q'_9) \\
& - \frac{R_2^{-1/2} R_z^{1/2} e^{(-\theta_2 + \theta_z)\mu'}}{(1/4 + \mu'^2)(a^2 + X_Y^2)} \left[ \left( \frac{1}{2} a^2 - \frac{1}{2} X_Y^2 - 2aX_Y \mu' \right) \sin q_{10} - (aX_Y + a^2 \mu' - X_Y^2 \mu') \cos q_{10} \right] \\
& + \frac{R_1^{-1/2} R_z^{1/2} e^{(-\theta_1 + \theta_z)\mu'}}{(1/4 + \mu'^2)(a^2 + X_Y^2)} \left[ \left( \frac{1}{2} a^2 - \frac{1}{2} X_Y^2 - 2aX_Y \mu' \right) \sin q'_{10} - (aX_Y + a^2 \mu' - X_Y^2 \mu') \cos q'_{10} \right] \Big\} d\theta \\
& + \text{REF}'_{fs} \quad \text{for } z > h_2,
\end{aligned} \tag{A7c}$$

---

where

$$\begin{aligned}
\text{REF}'_{fs} = & \int_0^{2\pi} \frac{iC'_\theta}{a^2 + X_Y^2} \left\{ R_2^{-3/2} R_z^{1/2} e^{(\theta_2 - 2\theta_0 + \theta_z)\mu'} (a \sin q_4 - X_Y \cos q_4) - R_1^{-3/2} R_z^{1/2} e^{(\theta_1 - 2\theta_0 + \theta_z)\mu'} (a \sin q'_4 - X_Y \cos q'_4) \right. \\
& - \frac{R_2^{-1/2} R_0^{-1} R_z^{1/2} e^{(\theta_2 - 2\theta_0 + \theta_z)\mu'}}{1/4 + \mu'^2} [(2a\mu'^2 - X_Y \mu') \sin q_5 - (a\mu' + 2X_Y \mu'^2) \cos q_5] \\
& + \frac{R_1^{-1/2} R_0^{-1} R_z^{1/2} e^{(\theta_1 - 2\theta_0 + \theta_z)\mu'}}{1/4 + \mu'^2} [(2a\mu'^2 - X_Y \mu') \sin q'_5 - (a\mu' + 2X_Y \mu'^2) \cos q'_5] \\
& - \frac{R_2^{-1/2} R_z^{-1/2} e^{(\theta_2 - 2\theta_0 + \theta_z)\mu'}}{1/4 + \mu'^2} \left[ \left( \frac{1}{4} a - a\mu'^2 + X_Y \mu' \right) \sin q_6 - \left( \frac{1}{4} X_Y - X_Y \mu'^2 - a\mu' \right) \cos q_6 \right] \\
& + \frac{R_1^{-1/2} R_z^{-1/2} e^{(\theta_1 - 2\theta_0 + \theta_z)\mu'}}{1/4 + \mu'^2} \left[ \left( \frac{1}{4} a - a\mu'^2 + X_Y \mu' \right) \sin q'_6 - \left( \frac{1}{4} X_Y - X_Y \mu'^2 - a\mu' \right) \cos q'_6 \right] \\
& + \frac{R_2^{-1/2} R_z^{1/2} e^{(\theta_2 - 2\theta_0 + \theta_z)\mu'}}{(1/4 + \mu'^2)(a^2 + X_Y^2)} \left[ \left( \frac{1}{2} a^2 - \frac{1}{2} X_Y^2 + 2aX_Y \mu' \right) \sin q_7 - (aX_Y - a^2 \mu' + X_Y^2 \mu') \cos q_7 \right] \\
& - \frac{R_1^{-1/2} R_z^{1/2} e^{(\theta_1 - 2\theta_0 + \theta_z)\mu'}}{(1/4 + \mu'^2)(a^2 + X_Y^2)} \left[ \left( \frac{1}{2} a^2 - \frac{1}{2} X_Y^2 + 2aX_Y \mu' \right) \sin q'_7 - (aX_Y - a^2 \mu' + X_Y^2 \mu') \cos q'_7 \right] \Big\} d\theta,
\end{aligned}$$

$$X_Y = x \cos \theta + y \sin \theta,$$

$$R_1 = \sqrt{a^2 + [(U_1 t - x) \cos \theta + (V_1 t - y) \sin \theta]^2},$$

$$\theta_1 = \arctan \frac{(U_1 t - x) \cos \theta + (V_1 t - y) \sin \theta}{a},$$

$$R_2 = \sqrt{a^2 + [(U_2 t - x) \cos \theta + (V_2 t - y) \sin \theta]^2},$$

$$\theta_2 = \arctan \frac{(U_2 t - x) \cos \theta + (V_2 t - y) \sin \theta}{a},$$

$$q_1 = \frac{3}{2} \theta_2 - \frac{1}{2} \theta_z + \mu' \ln \left( \frac{R_2}{R_z} \right),$$

$$q'_1 = \frac{3}{2} \theta_1 - \frac{1}{2} \theta_z + \mu' \ln \left( \frac{R_1}{R_z} \right),$$

$$q_2 = \frac{1}{2} \theta_2 + \frac{1}{2} \theta_z + \mu' \ln \left( \frac{R_2}{R_z} \right),$$

$$q'_2 = \frac{1}{2} \theta_1 + \frac{1}{2} \theta_z + \mu' \ln \left( \frac{R_1}{R_z} \right),$$

$$q_3 = \frac{1}{2} \theta_2 - \frac{1}{2} \theta_z + \mu' \ln \left( \frac{R_2}{R_z} \right),$$

$$q'_3 = \frac{1}{2} \theta_1 - \frac{1}{2} \theta_z + \mu' \ln \left( \frac{R_1}{R_z} \right),$$

$$q_4 = \frac{3}{2} \theta_2 - \frac{1}{2} \theta_z + \mu' \ln \left( \frac{R_2 R_z}{R_0^2} \right),$$

$$q'_4 = \frac{3}{2} \theta_1 - \frac{1}{2} \theta_z + \mu' \ln \left( \frac{R_1 R_z}{R_0^2} \right),$$

$$q_5 = \frac{1}{2} \theta_2 + \theta_0 - \frac{1}{2} \theta_z + \mu' \ln \left( \frac{R_2 R_z}{R_0^2} \right),$$

$$q'_5 = \frac{1}{2} \theta_1 + \theta_0 - \frac{1}{2} \theta_z + \mu' \ln \left( \frac{R_1 R_z}{R_0^2} \right),$$

$$q_6 = \frac{1}{2} \theta_2 + \frac{1}{2} \theta_z + \mu' \ln \left( \frac{R_2 R_z}{R_0^2} \right),$$

$$q'_6 = \frac{1}{2} \theta_1 + \frac{1}{2} \theta_z + \mu' \ln \left( \frac{R_1 R_z}{R_0^2} \right),$$

$$q_7 = \frac{1}{2} \theta_2 - \frac{1}{2} \theta_z + \mu' \ln \left( \frac{R_2 R_z}{R_0^2} \right),$$

$$q'_7 = \frac{1}{2} \theta_1 - \frac{1}{2} \theta_z + \mu' \ln \left( \frac{R_1 R_z}{R_0^2} \right),$$

$$q_8 = \frac{3}{2} \theta_2 - \frac{1}{2} \theta_z - \mu' \ln \left( \frac{R_2}{R_z} \right),$$

$$q'_8 = \frac{3}{2} \theta_1 - \frac{1}{2} \theta_z - \mu' \ln \left( \frac{R_1}{R_z} \right),$$



$$q_9 = \frac{1}{2}\theta_2 + \frac{1}{2}\theta_z - \mu' \ln\left(\frac{R_2}{R_z}\right),$$

$$q'_9 = \frac{1}{2}\theta_1 + \frac{1}{2}\theta_z - \mu' \ln\left(\frac{R_1}{R_z}\right),$$

$$q_{10} = \frac{1}{2}\theta_2 - \frac{1}{2}\theta_z - \mu' \ln\left(\frac{R_2}{R_z}\right),$$

$$q'_{10} = \frac{1}{2}\theta_1 - \frac{1}{2}\theta_z - \mu' \ln\left(\frac{R_1}{R_z}\right).$$

Integrations of (A5) and (A7) with respect to  $\theta$  are performed numerically using an extended trapezoidal rule.

#### REFERENCES

- Baik, J.-J., H.-S. Hwang, and H.-Y. Chun, 1999a: Transient critical-level effect for internal gravity waves in a stably stratified shear flow with thermal forcing. *Phys. Fluids*, **11**, 238–240.
- , —, and —, 1999b: Transient, linear dynamics of a stably stratified shear flow with thermal forcing and a critical level. *J. Atmos. Sci.*, **56**, 483–499.
- Booker, J. R., and F. P. Bretherton, 1967: The critical layer for internal gravity waves in a shear flow. *J. Fluid Mech.*, **27**, 513–539.
- Breeding, R. J., 1971: A non-linear investigation of critical levels for internal atmospheric gravity waves. *J. Fluid Mech.*, **50**, 545–563.
- Bretherton, F. P., 1966: The propagation of groups of internal gravity waves in a shear flow. *Quart. J. Roy. Meteor. Soc.*, **92**, 466–480.
- Eliassen, A., and E. Palm, 1960: On the transfer of energy in stationary mountain waves. *Geofys. Publ.*, **22**, 1–23.
- Grubišić, V., and P. K. Smolarkiewicz, 1997: The effect of critical levels on 3D orographic flows: Linear regime. *J. Atmos. Sci.*, **54**, 1943–1960.
- Han, J.-Y., and J.-J. Baik, 2009: Theoretical studies of convectively forced mesoscale flows in three dimensions. Part I: Uniform basic-state flow. *J. Atmos. Sci.*, **66**, 947–965.
- Jones, W. L., 1968: Reflexion and stability of waves in stably stratified fluids with shear flow: A numerical study. *J. Fluid Mech.*, **34**, 609–624.
- Keller, T. L., 1994: Implications of the hydrostatic assumption on atmospheric gravity waves. *J. Atmos. Sci.*, **51**, 1915–1929.
- Lin, Y.-L., 1987: Two-dimensional response of a stably stratified shear flow to diabatic heating. *J. Atmos. Sci.*, **44**, 1375–1393.
- , 2007: *Mesoscale Dynamics*. Cambridge University Press, 630 pp.
- , and S. Li, 1988: Three-dimensional response of a shear flow to elevated heating. *J. Atmos. Sci.*, **45**, 2987–3002.
- Pandya, R., and D. R. Durran, 1996: The influence of convectively generated thermal forcing on the mesoscale circulation around squall lines. *J. Atmos. Sci.*, **53**, 2924–2951.
- Shutts, G. J., 1995: Gravity-wave drag parametrization over complex terrain: The effect of critical-level absorption in directional wind-shear. *Quart. J. Roy. Meteor. Soc.*, **121**, 1005–1021.
- , 1998: Stationary gravity-wave structure in flows with directional wind shear. *Quart. J. Roy. Meteor. Soc.*, **124**, 1421–1442.
- , and A. Gadian, 1999: Numerical simulations of orographic gravity waves in flows which back with height. *Quart. J. Roy. Meteor. Soc.*, **125**, 2743–2765.
- Skamarock, W. C., M. L. Weisman, and J. B. Klemp, 1994: Three-dimensional evolution of simulated long-lived squall lines. *J. Atmos. Sci.*, **51**, 2563–2584.
- Song, I.-S., and H.-Y. Chun, 2005: Momentum flux spectrum of convectively forced internal gravity waves and its application to gravity wave drag parameterization. Part I: Theory. *J. Atmos. Sci.*, **62**, 107–124.
- Vosper, S. B., and S. D. Mobbs, 1998: Momentum fluxes due to three-dimensional gravity-waves: Implications for measurements and numerical modelling. *Quart. J. Roy. Meteor. Soc.*, **124**, 2755–2769.